

The Effect of Crystallographic Texture on the Constant-Stress, Constant-Heating-Rate Mechanical Test



S.L. SEMIATIN, N.C. LEVKULICH, and T.M. BUTLER

The effect of texture on plastic flow during the constant-stress, constant-heating-rate (CSCHR) mechanical test was established using Ti-6Al-4V sheet material with a strong basal-transverse starting texture. For this purpose, test samples were cut parallel to either the rolling direction (RD) or the long transverse direction (TD) of the sheet. CSCHR testing comprised preheating/soaking at 538 °C followed by heating at a constant rate of 75 °C/min while applying a constant true stress of 103, 172, or 276 MPa. The resulting plastic-strain-*vs*-time/temperature curves all exhibited a very low rate of straining at low temperatures followed by increasing strain rates at higher temperatures. For each applied stress level, the onset of high-strain-rate deformation occurred at a *higher* temperature for the TD sample than for the corresponding RD sample. The difference in RD and TD observations was successfully interpreted in terms of a constitutive relation incorporating a strength coefficient dependent on texture as quantified by measured Taylor Factors. A moderate effect of texture on cavitation and fracture was also noted. Specifically, cavities initiated along the boundaries between (hard) alpha particles and the (soft) beta matrix, leading to higher cavity growth rates and lower ductility in TD samples for a given applied stress. Such observations were ascribed to the texture dependence of local stress triaxiality and hence the cavity-growth rate. In addition, an observed effect of peak temperature on ductility was ascribed to the temperature dependence of the cavity growth rate.

<https://doi.org/10.1007/s11661-023-07270-y>

© The Minerals, Metals & Materials Society and ASM International 2023

I. INTRODUCTION

THE effect of crystallographic texture on mechanical response has been well known and documented for many years.^[1-4] In particular, its effect on yielding, plastic flow, and the formability of sheet metals at room temperature has been quantified for a variety of ferrous and nonferrous metals including low-carbon steels, nickel alloys, titanium alloys, etc. For low-carbon steels, for example, material composition and mill practices (*e.g.*, hot and cold rolling, annealing, *etc.*) are usually controlled to impart various degrees of texture and resulting normal (and planar) plastic anisotropy. Such

anisotropy can benefit subsequent sheet formability for deformation modes involving deep drawing, stretching, and combinations thereof.^[5-7]

Crystallographic texture in titanium alloys tends to have a greater effect on mechanical response than in cubic metals. For the near-alpha and alpha/beta titanium alloys that comprise a large portion of the total production of these materials, large plastic anisotropy is usually associated with the limited number of slip systems of hexagonal (alpha-phase) crystals in conjunction with differences in the critical resolved shear stress of the various slip (and twinning) systems that must be activated to accommodate imposed deformations. Rolling of plates and sheets of alloys such as Ti-6Al-4V often give rise to textures consisting of preferential alignment of the c-axes of alpha-phase crystallites parallel to the TD, the RD, or (sometimes) the normal direction (ND) of the finished product.^[8,9] These textures may produce undesirable RD-*vs*-TD differences in room-temperature yield strength, highly-anisotropic yield loci,^[10,11] and concomitant non-uniform flow during sheet forming (*e.g.*, ear formation during deep drawing) that necessitate careful consideration of pre-form/blank orientation relative to the die and finished-part geometry.

S.L. SEMIATIN and N.C. LEVKULICH are with the Air Force Research Laboratory, Materials and Manufacturing Directorate, Wright-Patterson Air Force Base, OH 45433-7817 and also with MRL Materials Resources LLC, Xenia Township, OH 45385. Contact e-mail: slseminat@gmail.com T.M. BUTLER is with the Air Force Research Laboratory, Materials and Manufacturing Directorate, Wright-Patterson Air Force Base.

Manuscript submitted October 2, 2023; accepted November 14, 2023.

Article published online December 24, 2023

The interaction of texture and plastic flow of titanium alloys at elevated temperatures has also been investigated. Specifically, texture can give rise to noticeable directionality in both yield strength and subsequent flow curves during hot working, especially for microstructures and process conditions outside the regime in which superplastic flow occurs.^[12–14] Limited mechanical anisotropy even during superplastic flow has also been observed.^[14] In such instances, however, the accommodation of plastic flow by sliding along alpha/beta boundaries and the accompanying rotation of alpha particles tend to randomize texture and thus reduce its effect on plastic flow.^[15–18]

Texture has also been found to affect deformation under intermediate-temperature creep conditions in alpha/beta titanium alloys. For instance, Li *et al.*^[19] observed a noticeable difference in behavior at 600 °C during creep testing of samples extracted along either the rolling or transverse directions of Ti60 alloy sheet with a strong basal-transverse texture.

The preponderance of investigations of the interaction of mechanical behavior and crystallographic texture have focused on deformation under nominally-isothermal (constant-temperature) conditions. Although such research has yielded much useful information, industrial processing and service conditions often involve temperature transients. Such transients may include temperature *decreases* during heat-treatment (*e.g.*, quenching), conventional forging (*e.g.*, die chill), and additive manufacturing and temperature *increases* due to frictional or deformation heating (*e.g.*, solid-state joining) or aerodynamic heating during high-speed flight. In these cases, the interpretation of plastic flow, let alone texture influences, can be substantially more difficult than that under isothermal conditions. In view of this complexity, a novel test technique was developed and applied recently for several aerospace alloys (Ti–7Al, Ti6242S, and superalloy 718).^[20] The technique consists of the application of a constant stress while heating at a constant rate. The strain-*vs*-time profiles resulting from the tests are readily converted to Arrhenius plots of $\ln(\text{strain rate})$ as a function of $1/T$, in which T denotes the instantaneous absolute temperature. By this means, material constitutive behavior (activation energy, stress exponent, *etc.*) can readily be determined from far fewer experiments than those required for characterization based on isothermal tests.

During the previous investigation of the constant-stress, constant-heating-rate (CSCHR) test,^[20] attention focused on the effect on plastic flow of various metallurgical phenomena such as the concurrent dissolution of a second phase and back stresses associated with a fine dispersion of second-phase particles. By contrast, the objective of present work was to establish the effect of crystallographic texture on CSCHR behavior. To this end, CSCHR experiments were conducted on Ti–6Al–4V specimens taken from the RD and TD directions of plate material which was pre-processed to have a fully-equiaxed microstructure and a strong basal-transverse texture. Measurements of initial and evolving textures were used to interpret the observed anisotropy in plastic flow.

II. MATERIALS AND PROCEDURES

A. Materials

The effect of crystallographic texture on plastic flow during CSCHR testing was quantified using the alpha/beta titanium alloy Ti–6Al–4V (hereafter referred to as Ti64). Its measured composition (in weight percent) was 6.37 Al, 3.89 V, 0.18 Fe, 0.14 O, 0.01 C, 0.007 N, 0.0049 H, balance titanium. The material was originally received as hot-rolled plate with a thickness of 15 mm; its beta-transus temperature (at which alpha + beta → beta) was 990 °C. A section of this plate measuring 75 mm length × 150 mm width was annealed at 960 °C for 2 hours and furnace cooled, thereby producing a microstructure of equiaxed alpha in a matrix of beta (Figure 1(a)). (In backscattered electron (BSE) images here and later, the darker phase is alpha, and the lighter phase is beta or transformed beta.) As determined by electron-backscatter diffraction (EBSD), the resulting alpha-phase texture consisted of a strong basal-transverse type ($\sim 24 \times$ random), *i.e.*, the $[0001]_z$ poles were aligned preferentially with the long transverse direction (TD) of the plate (Figure 1(b)). Despite the strong texture, the corresponding pole-density plot revealed noticeable “smearing” ($\sim \pm 10$ deg) about the perfect basal-transverse component (Figure 1(c)). Pole figures also revealed a secondary texture component comprising basal poles aligned with the RD (Figure 1(b)); its intensity was approximately 6 × random.

B. Experimental Procedures

Sheet tension samples for CSCHR tests were made *via* electrical discharge machining (EDM) the middle third of the plate, *i.e.*, that portion near the mid-thickness plane away from surface contamination. It was subsequently EDM sliced to produce sheet blanks with a thickness of 1.5 mm whose long direction was parallel to either the RD or TD of the original plate. The blanks were then EDM’ed to produce a sample geometry with a reduced section measuring 19.1-mm long × 3.2-mm wide (Figure 2). The dovetail portion of the shoulder (and corresponding segments of the TZM molybdenum tooling) were designed to enhance gripping along both the edges and the plan surfaces, thereby minimizing straining in the straight and tapered portions of the shoulders. Following EDM, the recast layer on both the plan surfaces and edges of the reduced section were removed using silicon carbide paper.

As in the previous work,^[20] CSCHR testing was performed in a computer-controlled Instron machine outfitted with an indirect-resistance Brew vacuum furnace (having tungsten-mesh heating elements) and TZM-molybdenum tooling. The test equipment and procedures were discussed in detail previously.^[20] In brief, a type-S thermocouple for temperature control was spot welded to the center of the gage section of each Ti64 sample. After mounting the sample into the test system, the vacuum furnace was evacuated to a pressure of $\sim 10^{-6}$ torr, heated to 538 °C, and soaked for 10

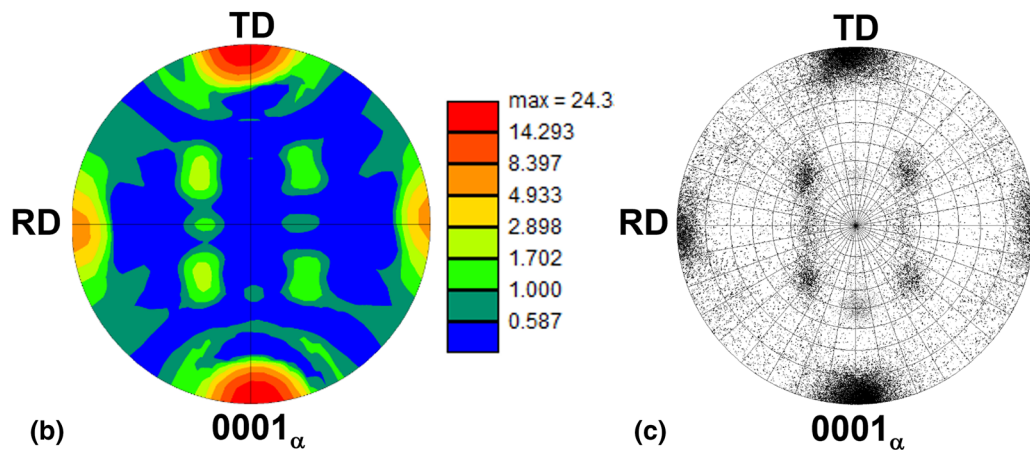
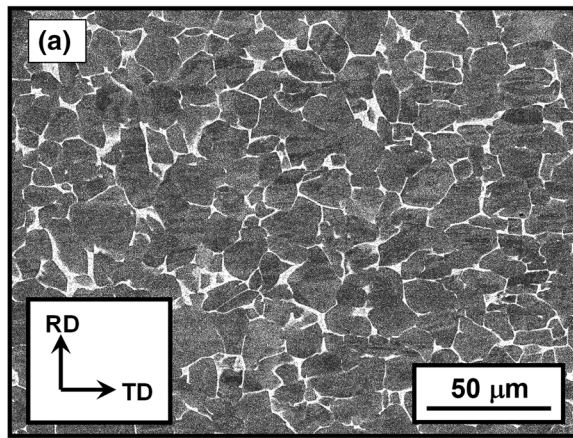


Fig. 1—Microstructure and texture of Ti-6Al-4V program material: (a) Backscattered electron (BSE) image and (b) $[0001]_{\alpha}$ pole figure and (c) pole-density plot determined using EBSD.

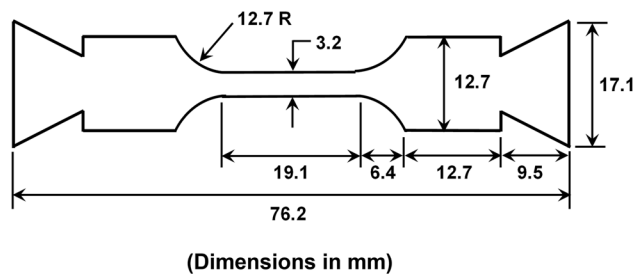


Fig. 2—Geometry of sheet tension sample used for CSCHR tests.

minutes to equilibrate the temperature of the sample and tooling. Following the soak period, an axial load corresponding to a true stress of either 103, 172, or 276 MPa was applied, and heating at a constant rate of 75 °C/min was begun and continued until sample failure. These test parameters enabled rapid evaluation of transient mechanical response, albeit at temperatures higher than those which are typical for Ti64.

As each sample was heated (and deformed plastically), the applied load was gradually reduced to maintain a nominally-constant true axial stress. To accomplish this, it was assumed that uniform *plastic*

deformation took place solely within the reduced section. This deformation was determined from linear-variable-differential-transformer (LVDT) measurements of the displacement of the sample plus load train, making suitable corrections for the extension associated with the mechanical compliance and thermal expansion of the sample and tooling/load cell. The latter quantity (the so-called “thermal compliance”) was determined from initial trials involving the heating of a test sample and the load train under a very small load during which plastic deformation of the sample was negligible. At each instant of time, the overall change in cross-sectional area associated with the axial plastic deformation and thermal expansion was determined and used to modify the applied load to maintain a constant axial true stress *via* a closed-loop control technique.

At the end of each experiment, rapid straining comprising localized (through-thickness) necking and failure occurred at which point the furnace power was turned off, and the sample was cooled to room temperature at a rate of ~55 °C/min. Faster cooling associated with water quenching could not be imposed due to the vacuum environment and fragility of the tungsten-mesh heating elements.

The effect of crystallographic texture on the high-temperature CSCHR behavior was compared to selected RD and TD tension test data measured at room temperature. These latter experiments were performed at a constant true strain rate of 0.005 s^{-1} .

The microstructures in broken test samples were determined using standard metallographic-preparation techniques and BSE imaging as described in prior work.^[21] Attention was focused on axial locations corresponding to 2 mm from the fracture (local axial strain denoted as ϵ_f) and to one-half of this strain ($\epsilon_f/2$); in all cases, local axial strains were determined from measurements of local sample width and thickness and application of the constant-volume assumption of plastic flow. The occurrence of cavitation during CSCHR testing was also quantified using high-resolution optical macrographs at the midplane of selected samples obtained with a Zeiss Axio Observer Z1m microscope with an Axio 503 Monochrome camera; the axial variation of cavity area fraction was then determined from the macrographs using Zeiss ZEN microscopy software. In addition, alpha-phase textures developed during deformation were determined via EBSD at the midplane for axial locations corresponding to ϵ_f and $\epsilon_f/2$ on each tested sample. At each location, EBSD was collected over an area measuring $250 \mu\text{m} \times 250 \mu\text{m}$ using a step size of $0.75 \mu\text{m}$. Because of the moderate cooling rate following fracture, any secondary alpha formed in the beta matrix during cooling (from the peak temperature achieved during heating and deformation) was very fine, thus resulting in poor-quality Kikuchi patterns that were not indexed. Thus, the EBSD textures measured at room temperature were representative of those formed due to deformation in the (primary) alpha phase during heating.

Taylor factors for the undeformed material and for the deformed samples at each of the two axial locations were estimated with the EDAX EBSD software package.^[22] Inputs to the calculations consisted of (i) the alpha-phase EBSD-measured textures, (ii) approximate values of the plastic anisotropy (r value), and (iii) an assumed ratio of the critical resolved shear stresses (CRSS's) for the hot deformation of alpha. Specifically, the value of r ($= d\epsilon_w/d\epsilon_t$, in which ϵ_w and ϵ_t denote the instantaneous values of the width and thickness strains, respectively, during deformation) was taken to be the ratio of the measured width and thickness strains at each of the two axial locations (noted above) in the fractured CSCHR samples. The ratio of the CRSSs for prism $\langle a \rangle$, basal $\langle a \rangle$, and $\langle c + a \rangle$ slip used in the EDAX TSL software was taken to be 1:1.5:3 based on the work in Reference 12. The Taylor factor for each measured texture (be it for the initial or deformed texture) was taken to be the ratio of the tension-axis yield strength divided by the CRSS for prism $\langle a \rangle$ slip.

C. Data Analysis

Measurements of average axial plastic strain vs time/temperature for each applied stress and test direction were converted to Arrhenius plots ($\ln(\text{strain rate})$ vs $1/T(\text{K})$). The applicability of using average axial strain

(and strain rate) in the analysis was justified using flow-localization calculations such as those described in Appendix A. Differences in behavior between the RD and TD results were interpreted in terms of an engineering constitutive relation presented in Section IV (Discussion) which included a Taylor-factor-dependent strength coefficient, activation energy for plastic flow, and strain rate sensitivity exponent (m).

III. RESULTS

A. Strain-vs-Time/Temperature Measurements

Plastic-strain-vs-temperature plots for the Ti64 program material (Figure 3(a)) were similar to those found previously for Ti-6Al-2Sn-4Zr-2Mo-0.1Si with an equiaxed-alpha microstructure.^[20] (Because the heating rate was constant, the corresponding strain-vs-time plots were similar except for linear scaling of the abscissa, and thus are not shown here for brevity.) In all cases, straining of the Ti64 samples was very limited during the early part of the heating cycle, *i.e.*, at low temperatures/short times. As the temperature and time increased, the strain increased in an approximately exponential fashion. As expected, the temperature at which the straining accelerated increased with decreasing applied stress. Moreover, for each level of stress, the rapid straining of the RD sample initiated at a lower temperature than the corresponding TD sample. This difference in temperature for rapid straining was due to differences in texture strengthening for the RD and TD samples and is discussed in Section IV.

Arrhenius plots ($\ln \dot{\epsilon}$ vs $1000/T(\text{K})$), in which $\dot{\epsilon}$ denotes the plastic strain rate) derived from the plastic strain vs temperature/time results (Figure 3(b)) highlighted the difference in RD-vs-TD behavior during CSCHR testing. For each stress level, the RD plot lay to the right of that for the TD experiment, *i.e.*, at higher values of $1/T$ or lower values of T . The magnitudes of such $1/T$ “offsets” at specific levels of $\ln \dot{\epsilon}$ are summarized in Table I. The various plots also had somewhat different shapes ranging from nearly linear to those with a gradual curvature. Because the slope connotes an apparent activation energy for plastic flow normalized by the gas constant *i.e.*, Q_{app}/R , the nearly-linear behaviors suggested a nearly-constant activation energy whereas those with a curvature exhibited a variation with temperature. As discussed in Reference 20, the latter trend can be ascribed to a temperature range over which the volume fractions of the phases in a two-phase alloy vary markedly, thus giving rise to a so-called “mechanical contribution” to the activation energy.^[23]

The results in Figure 3(b) also show a “jagged” nature at low values of $\ln \dot{\epsilon}$. Such observations resulted from the low resolution of strain at small tension displacements and the accompanying “noise” in taking the derivative of strain-vs-time plots here.

Noticeable directionality was also noted in room-temperature flow curves measured along the RD and TD (Figure 4). The yield strength (proportional limit) and flow stress at given levels of strain were approximately

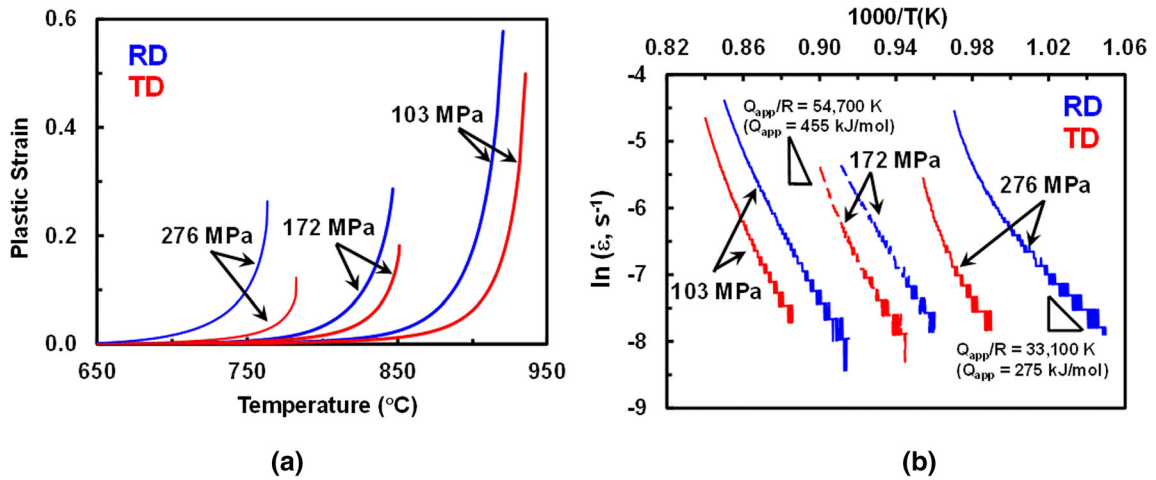


Fig. 3—Plastic flow determined from constant-stress ($\sigma = 103, 172,$ or 276 MPa), constant-heating-rate (75 °C/min) experiments on Ti64 samples pulled along the RD or TD: (a) Plastic strain as a function of temperature and (b) $\ln \dot{\epsilon}$ as a function of $1000/T$.

Table I. Measured Values of the Inverse-Temperature Offset, $(1000/T_{RD}) - (1000/T_{TD})$, in $\ln \dot{\epsilon}$ vs $1/T$ Plots as a Function of Stress Level and Strain Rate

| Stress (MPa) | $\ln \dot{\epsilon}$ (s^{-1}) | Average $1000/T$ (K) | T(°C) | $(1/T)_{RD} - (1/T)_{TD} \times 1000$ (K^{-1}) |
|--------------|-----------------------------------|----------------------|-------|--|
| 103 | -5 | 0.85 | 903.5 | 0.0136 |
| 103 | -6 | 0.865 | 883.1 | 0.0172 |
| 103 | -7 | 0.884 | 858.2 | 0.0188 |
| 172 | -5.5 | 0.908 | 828.8 | 0.012 |
| 172 | -6.5 | 0.924 | 809.3 | 0.0184 |
| 172 | -7.5 | 0.946 | 784.1 | 0.0196 |
| 276 | -5.5 | 0.968 | 760.1 | 0.0292 |
| 276 | -6.5 | 0.985 | 742.2 | 0.0412 |
| 276 | -7.5 | 1.011 | 716.1 | 0.0532 |

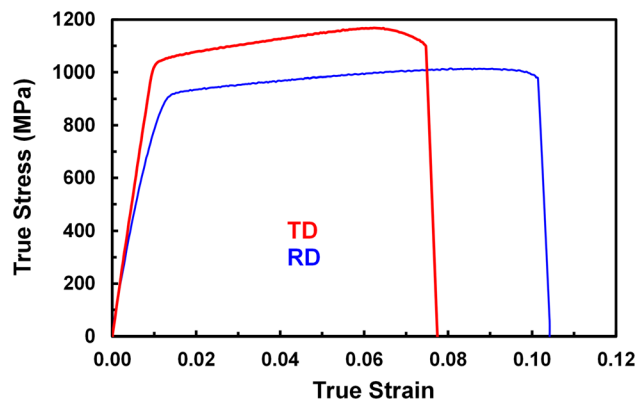


Fig. 4—Room-temperature flow curves of textured Ti64 deformed in uniaxial tension at a strain rate of 0.005 s^{-1} along either the RD or TD.

10 to 15 pct. higher for testing along the TD in comparison to that for RD. Testing along the TD also gave rise to a noticeably higher Young's modulus. The measured values of modulus (~ 115 GPa for the TD, ~ 80 GPa for the RD) should be considered as approximate

because strain was determined without an extensometer on the reduced section. Nevertheless, the observed trends appeared reasonable in view of the strong basal-transverse texture and the well-known effect of texture on modulus.^[8]

B. Microstructure Observations

Observations of deformed microstructures and resulting textures provided insight into the nature of plastic flow during the CSCHR testing of Ti64 with an initial fully-equiaxed microstructure.

The microstructure of CSCHR samples pulled to failure along the RD and cooled at a rate of ~ 55 °C/min following testing (e.g., Figure 5 for an applied stress of 103 MPa) exhibited substantially less primary alpha (~ 65 pct) compared to that in the starting (room-temperature) microstructure (~ 92 pct) (Figure 1(a)). Because the initial soak temperature (538 °C) was relatively low for the dissolution of a measurable amount of alpha,^[21] it may be concluded that the majority of the reduction in the volume fraction of alpha in CSCHR samples occurred *during* heating with

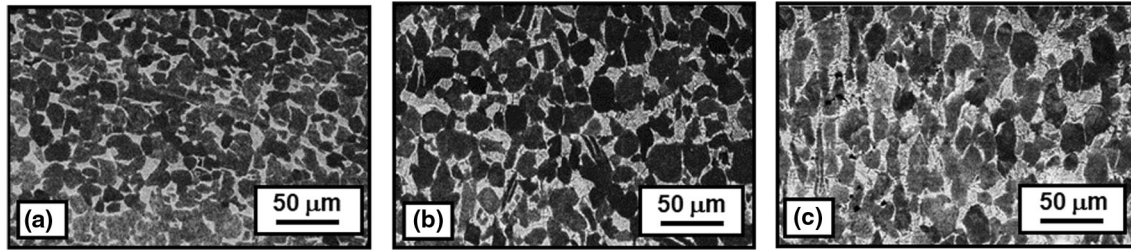


Fig. 5—BSE images of Ti64 CSCHR sample RD-1 deformed at a constant stress of 103 MPa and heating rate of 75 °C/min for local regions in which the axial strain was (a) 0 (shoulder), (b) 0.39, or (c) 0.78. In all images, the vertical direction corresponds to the tension axis/RD, and the horizontal direction is parallel to the width direction/TD.

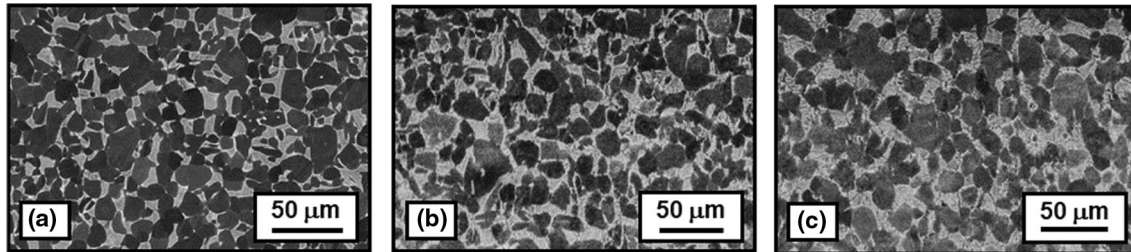


Fig. 6—BSE images of Ti64 CSCHR sample TD-1 deformed at a constant stress of 103 MPa and heating rate of 75 °C/min for local regions in which the axial strain was (a) 0 (shoulder), (b) 0.32, or (c) 0.63. In all images, the vertical direction corresponds to the tension axis/TD, and the horizontal direction is parallel to the width direction/RD.

perhaps a small amount of re-growth during final cooling. Equally, if not more importantly, the alpha-phase particles in the deformed samples showed an elongation along the tension direction (Figures 5(b) and (c)). The effect was especially noticeable near the fracture at which the local strain was the largest (Figure 5(c)). Thus, it may be surmised that the plastic flow generated during the present Ti64 CSCHR tests was probably dominated by the glide and climb of dislocations rather than by grain-boundary/interphase sliding typical of superplasticity which would likely maintain an equiaxed microstructure.

As will be discussed in Section III-C, a second factor contributing to the shape of the alpha particles generated during CSCHR testing was the plastic anisotropy. Low r values ($\ll 1$) would limit straining along the width direction during tension testing and hence could accentuate the elongated appearance of alpha particles in metallographic sections containing the width direction.

Alpha-particle elongation was also seen in samples pulled along the TD (e.g., Figure 6(c) for a TD sample subjected to a stress of 103 MPa). The degree of elongation was less noticeable than that for the RD samples, partly because of the lower failure strains (Figure 3(a)). Failure at lower strains (and low temperatures), as observed for RD and TD samples subjected to CSCHR testing using stresses of 172 or 276 MPa (Figure 3(a)), also reduced the observed amount of alpha-particle elongation seen in corresponding BSE images (not shown).

C. Texture and Plastic Anisotropy Measurements

Pole figures, r -value measurements, and Taylor-factor estimates gave insight into texture evolution during CSCHR tests for the Ti64 program material. Attention was focused on RD and TD samples subjected to the lowest and highest stresses (i.e., 103 and 276 MPa). Pole figures determined at two locations in each specimen ($\varepsilon = \varepsilon_f/2$ and ε_f) indicated marked changes in texture associated with deformation during each CSCHR test. The changes were greatest for the RD and TD samples subjected to an applied stress of 103, which underwent the largest strain prior to failure, and thus are summarized here. For the sample which was deformed along the RD, $\varepsilon_f \sim 0.78$ (Table II), and the strong initial TD texture component was reduced in intensity from $\sim 24 \times$ random to $\sim 11 \times$ random or $\sim 8 \times$ random after strains of $\varepsilon_f/2$ and ε_f , respectively (Figures 7(a) and (b)). In addition, the intensity of the weaker initial RD component was also reduced or almost totally eliminated. For the sample which was deformed along the TD, $\varepsilon_f \sim 0.63$ (Table II), and the strong initial TD texture component was also noticeably reduced in intensity from $\sim 24 \times$ random to $\sim 17 \times$ random or $\sim 5 \times$ random after strains of $\varepsilon_f/2$ and ε_f , respectively (Figures 7(c) and (d)). In this case, the reduction was associated with substantial additional smearing of the principal texture component about the TD/tension axis, especially for $\varepsilon = \varepsilon_f$. Such changes were likely due to the activation of prism $\langle a \rangle$ (or basal $\langle a \rangle$) slip systems for alpha particles initially oriented several degrees or more away from the perfect c -axis orientation.^[24,25]

Table II. Fracture Strains (ϵ_f), r-Values, and Average Taylor Factors (M) for Ti64 CSCHR Experiments

| ID | Test Direction | Stress (MPa) | ϵ_f | M ($\epsilon = 0$) | r ($\epsilon_f/2$) | M ($\epsilon_f/2$) | r (ϵ_f) | M (ϵ_f) |
|------|----------------|--------------|--------------|----------------------|----------------------|----------------------|--------------------|--------------------|
| RD-1 | RD | 103 | 0.78 | 4.5 | 0.26 | 4.4 | 0.31 | 4.3 |
| TD-1 | TD | 103 | 0.63 | 5.59 | 0.58 | 5.2 | 0.63 | 4.95 |
| RD-4 | RD | 276 | 0.36 | 4.4 | 0.17 | 4.5 | 0.20 | 4.36 |
| TD-4 | TD | 276 | 0.03 | 5.61 | — | — | 0.79 | — |

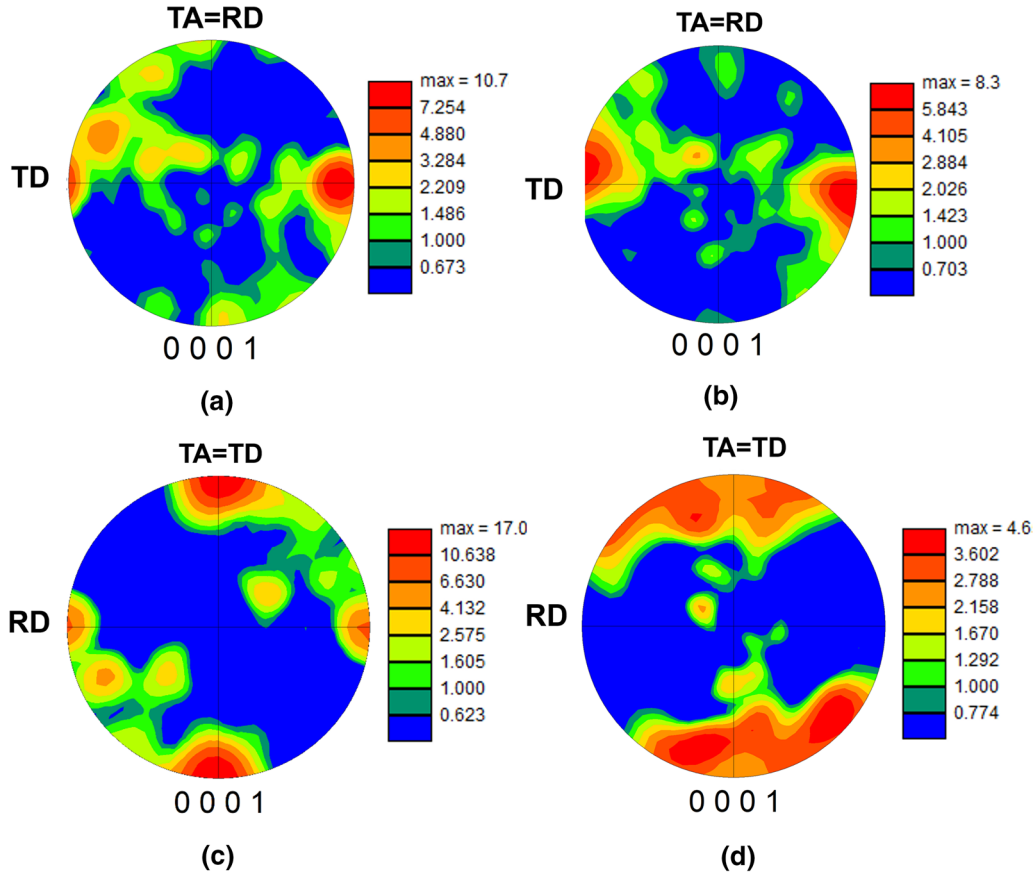


Fig. 7—Pole figures for samples (a, b) RD-1 and (c, d) TD-1 at locations at which the local strain (Table II) was equal to (a, c) $\epsilon_f/2$ or (b, d) ϵ_f .

The effect of texture on plastic anisotropy during CSCHR testing of Ti64 was evident from the r-value measurements (Table II). For samples pulled along the RD, the r values were very small, lying in the range of 0.17 to 0.31. Such low values can be rationalized on the basis of the preferential orientation of hard, c-axis alpha-phase particles along the TD/width direction of such tension specimens. Deformation along the width direction was thus limited, thereby forcing large thickness-direction straining to maintain the incompressibility associated with plastic flow. On the other hand, the r values for specimens pulled along the TD were larger (~ 0.60), but still less than unity. In these cases, the weaker c-axis texture component along the RD/width direction of tension specimens oriented thusly can be surmised to have limited width-direction straining to a

modest extent relative to thickness-direction deformation during CSCHR tests on such TD-oriented samples.

Taylor factors (M) based on the measured textures and assumed strain (increment) tensors corresponding to uniaxial tension (*i.e.*, those mirroring deformation approximated by the measured r values) are also listed in Table II. First, the variation of M with test direction exhibited a qualitative trend expected based on the starting texture. That is to say, for CSCHR tension along the TD (*i.e.*, pulling parallel to the principal c-axis texture component) gave rise to higher Taylor factors (of the order of 5.5) compared to those for tension along the RD (~ 4.5). Secondly, the data in Table II indicated a broad decrease in M with increasing strain, especially for the RD and TD tests involving an imposed stress of 103 MPa, for which the levels of imposed strain prior to failure were greatest. The values of M reported here

were used to interpret the plastic-strain-*vs*-temperature observations (Section IV-A).

D. Failure/Cavitation Observations

Ductility data (Figure 3(a), Table II) also showed noticeable trends with respect to applied stress and test orientation. The failure strain and failure temperature both decreased as the applied stress increased (Figure 3(a)). Furthermore, each TD sample underwent a lower elongation and broke at a higher temperature than the corresponding RD sample for a given applied stress. The ϵ_f data (Table II) quantified these observations as well.

Observations of cavitation at two levels of strain ($\sim 0.5 \epsilon_f$ and ϵ_f) for RD and TD samples tested using an applied stress of 103 MPa provided insight into the anisotropy of ductility (Figures 8, 9). Each observation comprised a tension-axis inverse-pole-figure (IPF) map to show the local orientation of alpha particles adjacent to cavities and an image-quality (IQ) map to highlight local deformation. For the RD sample, the IPF map for the lower strain level showed relatively-fine cavities and suggested a range of alpha-particle orientations adjacent to each cavity (Figure 8(a)). The corresponding IQ map (Figure 8(b)) revealed that cavities appeared to form adjacent to (largely-featureless) alpha particles in matrix regions containing a fine transformation product (likely developed during cool down); such matrix regions were

single-phase beta at high temperatures. These observations suggested that cavitation was heavily influenced by the flow-stress mismatch between (harder) alpha particles and the (softer) beta matrix, thus giving rise to substantial, local stress triaxiality. The IPF and IQ maps for the RD sample at the higher strain level (Figures 8(c) and (d)) underscored these conclusions. The presence of hard-oriented (red/basal-oriented) alpha particles adjacent to a number of cavities in the IPF map (circled in Figure 8(c)) suggested the exacerbation of cavitation by a large flow-stress mismatch. In the high-strain IQ map for the RD sample (Figure 8(d)), the presence of large voids (within what were beta-matrix regions at high temperature) suggested plasticity-controlled cavity growth in the softer of the two phases.

For the corresponding TD sample tested using an applied stress of 103 MPa, the overall trends were similar (Figure 9). The major difference consisted of the very strong initial texture of the primary-alpha particles with their basal poles parallel to the tension axis, thus representing a hard orientation for this phase. Although the cavities in the TD sample also formed adjacent to the primary alpha particles and grew into what was the beta matrix at high temperature (Figures 9(b) and (d)), it may be hypothesized that the large volume fraction of initially basal-oriented alpha particles accelerated cavity initiation and growth in the TD sample, thus leading to a smaller ductility than the corresponding RD sample. However, this trend may have been mitigated somewhat

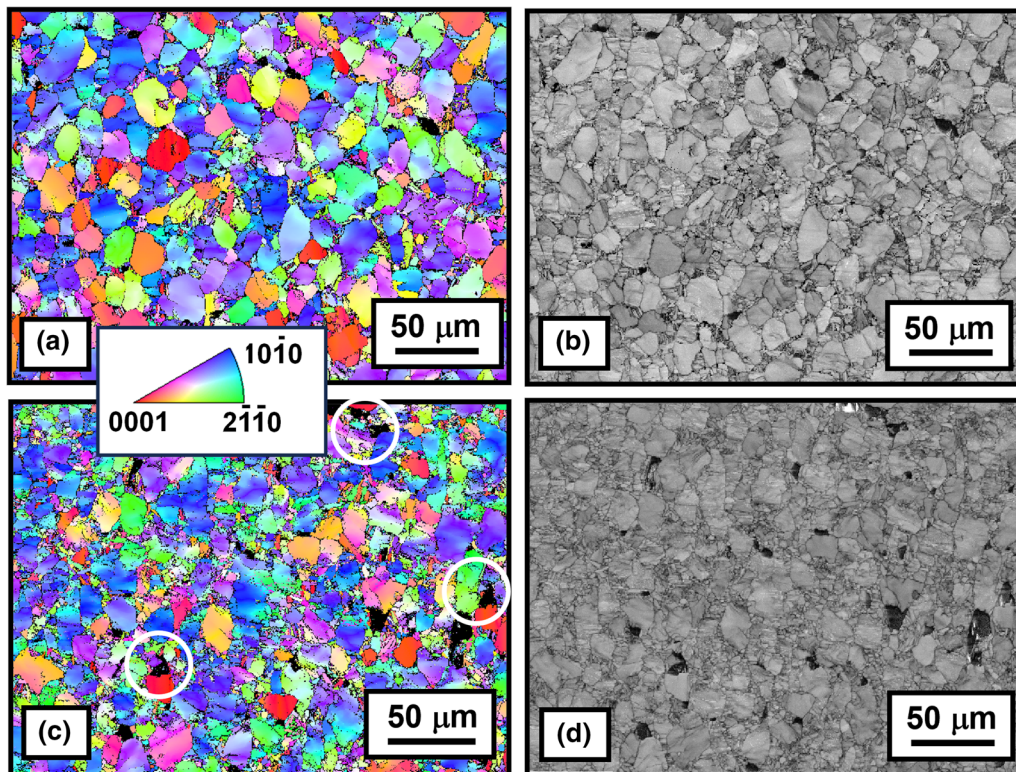


Fig. 8—Microstructure and cavitation observations for an RD CSCHR specimen pulled using a constant stress of 103 MPa and heating rate of 75 °C/min: (a, c) tension-direction IPF maps and (b, d) IQ maps. Data were obtained at locations corresponding to (a, b) $\epsilon_f/2 = 0.39$ or (c, d) $\epsilon_f = 0.78$. In all images, the vertical direction corresponds to the tension axis/RD, and the horizontal direction is parallel to the width direction/TD.

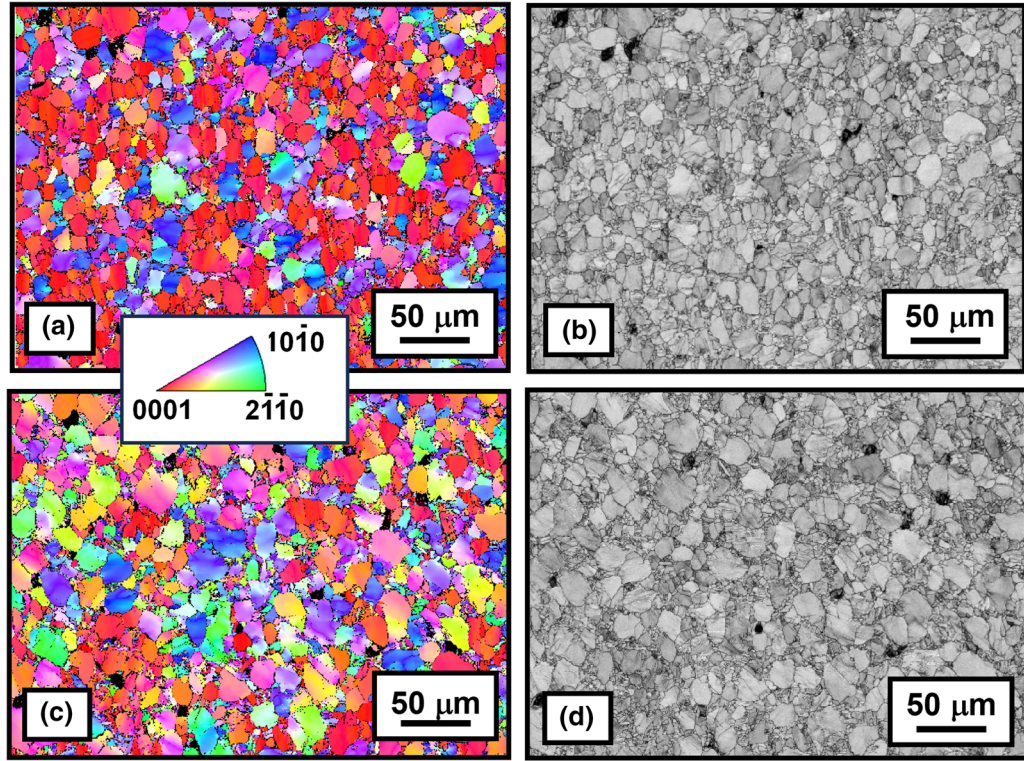


Fig. 9—Microstructure and cavitation observations for a TD CSCHR specimen pulled using a constant stress of 103 MPa and heating rate of 75 °C/min: (a, c) tension-direction IPF maps and (b, d) IQ maps. Data were obtained at locations corresponding to (a, b) $\epsilon_f/2 = 0.315$ or (c, d) $\epsilon_f = 0.63$. In all images, the vertical direction corresponds to the tension axis/TD, and the horizontal direction is parallel to the width direction/RD.

by the rotation of alpha particles away from their initial basal orientations during tension, thus reducing stress triaxiality and its deleterious effect on cavitation.

IV. DISCUSSION

Observations of anisotropy in plastic flow and cavitation made in this work were interpreted in terms of the effect crystallographic texture on constitutive behavior and local stress state.

A. Interpretation of Anisotropy in Plastic Flow

To obtain insight into the effect of texture on the anisotropy of plastic flow, the flow stress of Ti64, σ , was taken to be a rule-of-mixtures average of the flow stresses of the individual alpha and beta phases (σ_α , σ_β), *i.e.*,

$$\sigma = f_\alpha \sigma_\alpha + f_\beta \sigma_\beta = f_\alpha \sigma_\alpha + (1 - f_\alpha) \sigma_\beta, \quad [1]$$

in which f_α denotes the volume fraction of alpha. At a given strain rate, the flow stress of the beta phase is approximately one-third that of the alpha phase.^[26] Furthermore, for the temperature regime in which most of the deformation occurred in the present experiments (*i.e.*, 700 to 900 °C, Table I), f_α was in the range of 0.6 to 0.9 (Appendix B, Figure B1). Assuming that deformation of the two-phase mixture can be approximated by

an isostrain/isostrain-rate behavior,^[21] the principal contribution to the overall flow stress was thus due to deformation of the alpha phase.

Neglecting the flow-stress contribution due to deformation of the beta phase (because of its considerably lower flow stress and low volume fraction) enables the derivation of a simple, semi-quantitative relation for the effect of the texture of the alpha phase on the “offset” in the $\ln \dot{\epsilon}$ vs $1000/T(K)$ plots in Figure 3(b). For this purpose, the flow stress was taken to depend on texture through the Taylor factor of the alpha phase, M , in a phenomenological constitutive relation of the following form:

$$\sigma = CM\dot{\epsilon}^m \exp\left(\frac{mQ_{app}}{RT}\right) \quad [2]$$

in which C is a constant, $\dot{\epsilon}$ is strain rate, m is the strain rate sensitivity, Q_{app} is an *apparent* activation energy for plastic flow, R is the gas constant, and T is absolute temperature. Because of the two-phase nature of Ti64 and the so-called “mechanical” contribution,^[20,23] it should be borne in mind that the apparent activation energy Q_{app} may not have a physical relation to a specific mechanism such as creep or solute diffusion as is often found in the interpretation of observations for single-phase alloys.

After taking the natural logarithm of both sides, the variational form of Eq. [2] is as follows:

$$\delta \ln \sigma = \delta \ln M + \delta \ln \dot{\epsilon}^m + \delta \left(\frac{m Q_{app}}{RT} \right) \quad [3]$$

For a given applied stress σ and fixed $\ln \dot{\epsilon}$, a relation between variations in the Taylor factor and $(1/T)$ (after rearranging) is obtained, *i.e.*,

$$\frac{1}{T_1} - \frac{1}{T_2} = \left(\frac{R}{m Q_{app}} \right) \ln(M_2/M_1) \quad [4a]$$

Taking 1 \equiv RD and 2 \equiv TD, the final expression is then

$$\frac{1}{T_{RD}} - \frac{1}{T_{TD}} = \left(\frac{R}{m Q_{app}} \right) \ln(M_{TD}/M_{RD}) \quad [4b]$$

Equation [4b] was applied to obtain theoretical estimates of inverse-temperature offsets as a function of Q_{app} , m , and M_{RD}/M_{TD} (Table III), which could be compared to measured values (Table I). For each stress level, Q_{app}/R was obtained from the slope of $\ln \dot{\epsilon}$ vs $1000/T$ plots (Figure 3(b)). The nearly-linear slopes provided a single Q_{app}/R (54,700 K) for applied stresses of 103 and 172. For the applied stress of 276 MPa, two values (54,700 K and 33,100 K) were used to bound the slopes of the non-linear plots. Values of m ($= \partial \ln \sigma / \partial \ln \dot{\epsilon}$) were obtained by comparing the $\ln \dot{\epsilon}$ vs $1000/T$ plots for a specific tension axis (*i.e.*, RD or TD) at given values of $1/T$ and different applied stresses. The m 's so obtained (0.18 to 0.23 at $T \sim 800$ °C to 900 °C and 0.12 to 0.15 at $T \sim 700$ °C to 750 °C) were similar to those measured from continuous flow curves and/or strain-rate jump tests for Ti64 and Ti-6Al-2Sn-4Zr-2Mo-0.1Si at various temperatures.^[21,27] Last, the values of M_{TD}/M_{RD} of 1.24 and 1.18 were obtained from Table II for undeformed and deformed samples. With these input parameters, model predictions of the inverse-temperature offset for RD vs TD samples tested at given stress levels (Table III) showed good agreement with measurements (Table IV).

Equation [4b] reveals that the inverse-temperature offset (and the corresponding temperature offset on

plastic-strain-vs-temperature plots) are very sensitive to the ratio of the Taylor factors along the orthogonal TD and RD directions. Because of the large difference in the CRSS for pyramidal $\langle c+a \rangle$ slip and prism $\langle a \rangle$ slip, alpha/beta (and near-alpha) titanium sheet alloys with a very sharp texture can exhibit much larger differences in flow behavior for TD vs RD tests than those observed here. For example, for M_{TD}/M_{RD} equal to 2.0 or 3.0 (rather than ~ 1.24 , as in the present program material), the inverse-temperature offsets would be respectively ~ 3 or 5 times that measured here.

B. Failure Behavior

The total elongations exhibited by the Ti64 CSCHR samples with the equiaxed-alpha microstructure were less than those predicted by flow-localization models^[28] and the classical Woodford correlation to the strain rate sensitivity.^[29] For samples tested using stresses of 103 and 276 MPa, for example, the *measured* (engineering) RD elongations were ~ 78 and ~ 30 pct., respectively, and even less for the TD samples. Per the analysis of Ghosh and Ayres,^[28] the “terminal” rate sensitivity near the *end* of each corresponding CSCHR test (0.23 and 0.12, respectively) was used to estimate the expected elongation from the Woodford plot.^[29] These elongations were 106 pct. and 35 pct., respectively, or values *exceeding* the present measurements. Thus, it was concluded that Ti64 CSCHR failures were controlled by fracture prior to flow localization. This conclusion was also supported by macroscopic failures lying perpendicular to the tension axis, rather than at an angle corresponding to the zero-extension (through-thickness, localized-necking) direction in each specimen.

Metallographic observations revealed that the fractures were ductile, *i.e.*, controlled by cavity initiation, growth, and coalescence (Figures 8 and 9). From a broad perspective, the failure strain ϵ_f decreased monotonically with increasing stress (Figure 3(a)). However, the product of stress and failure strain (Table II) showed a wide variation as a function of temperature. This finding suggested that *macroscopic* plastic work cannot provide a reliable metric for fracture, let alone for the

Table III. Model predictions of the inverse temperature offset, $(1000/T_{RD}) - (1000/T_{TD})$, as a function of Q_{app} , M_{RD}/M_{TD} , and m

| Stress (MPa) | Q_{app}/R (K) | M_{TD}/M_{RD} | m | $(1/T)_{RD} - (1/T)_{TD}$ X1000 (K ⁻¹) |
|--------------|--------------------|-----------------|------|--|
| 103 | 54,700 | 1.242 | 0.18 | 0.0218 |
| 103 | 54,700 | 1.182 | 0.18 | 0.0168 |
| 103 | 54,700 | 1.242 | 0.23 | 0.0174 |
| 103 | 54,700 | 1.182 | 0.23 | 0.0134 |
| 172 | 54,700 | 1.242 | 0.18 | 0.0218 |
| 172 | 54,700 | 1.182 | 0.18 | 0.0168 |
| 276 | 33,100 | 1.242 | 0.15 | 0.0439 |
| 276 | 33,100 | 1.182 | 0.15 | 0.0338 |
| 276 | 33,100 | 1.242 | 0.12 | 0.0544 |
| 276 | 33,100 | 1.182 | 0.12 | 0.0419 |

observed differences in RD vs TD behavior. Therefore, a more-detailed explanation based on the discrete mechanisms involved in cavitation (and the imposed temperature history) appears to be required.

Measurements of the cavity volume fraction C_v as a function of strain (e.g., Figure 10 for RD and TD samples subjected to CSCHR testing using a stress of 103 MPa) revealed approximately linear behaviors when plotted in a semi-logarithmic fashion. Using an engineering (operational) definition of $\ln C_v$ in the range of -7 to -6 to signify cavity nucleation, the corresponding initiation strains lay in the range of approximately 0.15 to 0.39 for RD samples (Figure 10(a)) and 0.28 to 0.42 for TD samples (Figure 10(b)) tested using a stress of 103 MPa. The broad similarity in initiation strain for RD and TD samples may perhaps be rationalized on the basis of the large difference in flow stress between the alpha and beta phases per se, and not necessarily between alpha particles with different orientations. Nevertheless, alpha-particle orientation did appear to play some role in cavity initiation based on observations of a large number of voids adjacent to an alpha particle with a hard orientation (c-axis parallel to the tension axis) shown as red in inverse-pole-figure maps (e.g., Figures 8(c) and 9(c)).

The slopes of the $\ln C_v$ -vs-strain plots for RD and TD samples showed a measurable difference, thus suggesting differences in *cavity-growth* behavior.^[30] For example, samples tested along the RD or TD using a stress of 103 MPa exhibited slopes of ~ 4.4 and 7.0 , respectively.

Table IV. Comparison of Measurements and Model Predictions of the Inverse-Temperature Offset, $(1000/T_{RD}) - (1000/T_{TD})$, for RD and TD Samples

| Stress (MPa) | Measurement (K^{-1}) | Model Prediction (K^{-1}) |
|--------------|--------------------------|-------------------------------|
| 103 | 0.0136–0.0188 | 0.0134–0.0218 |
| 172 | 0.012–0.0196 | 0.0168–0.0218 |
| 276 | 0.0292–0.0532 | 0.0338–0.0544 |

These slopes represent the *apparent* cavity growth rate η_{app} in the equation $C_v = C_{v0} \exp(\eta_{app}(\epsilon - \epsilon_{init}))$. To interpret the source of the difference between the RD and TD behaviors, however, it is better to examine the effect of texture on the growth of individual cavities. For this purpose, values of the growth rate of an individual cavity η deformed under conditions of uniaxial tension, denoted as η , can be related to η_{app} via the simulation results reported in Reference 31. For cavity nucleation rates of the order of $(10 \text{ to } 50) \times 10^4 \text{ cav/mm}^3/\text{unit strain}$, such as those measured in the present work for both RD and TD samples, $\eta/\eta_{app} \sim 0.9$ for both test orientations. Thus, an alternate source of the difference in the slopes in Figure 10 must be sought.

One alternative is the difference in stress triaxiality (\equiv ratio of mean to effective stress) generated at the scale of the alpha particles. Various theoretical models in conjunction with an analysis of measurements on a number of metallic materials have shown that an increase in triaxiality from 0.33 (pure uniaxial tension) to ~ 0.65 would increase the cavity growth rate by ~ 60 pct,^[32] or the approximate magnitude exhibited by the RD vs TD samples in Figure 10. Future analytical work will thus focus on quantifying the local triaxiality generated around cavities in the present experiments.

In a similar vein, it is likely that the temperature dependences of the cavity-growth rate (averaged over the temperature interval in which the bulk of deformation occurs) and the overall ductility are interrelated. For deformation under uniaxial-tension conditions, $\eta \approx 1/m$.^[30] In particular, for Ti64 and Ti-6Al-2Sn-4Zr-2Mo-0.1 Si, m decreases by a factor of ~ 2 when the temperature decreases from ~ 900 °C to 750 °C.^[21,27] Assuming that the local triaxiality is independent of temperature, a similar *increase* in the value of the cavity growth rate from ~ 900 °C to 750 °C may also be expected, thus giving rise to correspondingly lower ductility with decreasing temperature, as was observed (Figure 3(a)).

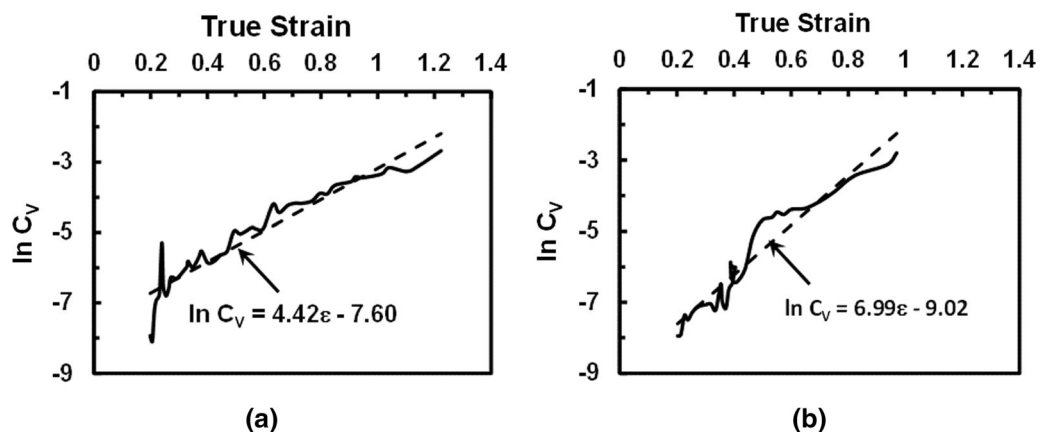


Fig. 10—Plots of $\ln C_v$ vs true strain for CSCHR tests using a stress of 103 MPa for samples tested along the (a) RD or (b) TD.

V. SUMMARY AND CONCLUSIONS

Constant-stress, constant-heating-rate (CSCHR) tension tests were conducted on Ti-6Al-4V (Ti64) samples with a strong crystallographic texture. The following conclusions were drawn from this work:

1. Deformation under CSCHR conditions for a textured material is delayed to higher temperatures when testing along a crystallographically-stronger direction. For Ti64, noticeable straining starts to occur at higher temperatures for tests oriented along the hard, c-axis direction compared to those for samples oriented along “softer” (lower Taylor-factor) directions.
2. The “offset” in semi-log plots of plastic strain rate vs inverse temperature for textured materials tested along two different directions is inversely proportional to the strain-rate sensitivity and apparent activation energy and directly proportional to the natural logarithm of the ratio of the Taylor factors along the two directions.
3. Failure during CSCHR tension testing of Ti64 at high temperatures is controlled by the nucleation, growth, and coalescence of cavities within (soft) beta-matrix regions in the immediate vicinity of the (hard) alpha particles. For a given applied stress, texture tends to exert an effect on ductility through its impact on local stress triaxiality and the cavity growth rate. Temperature plays an important role in controlling ductility during CSCHR tension testing of Ti64 as well, largely because of the temperature dependence of the strain rate sensitivity and corresponding values of the cavity-growth parameter.

ACKNOWLEDGMENTS

This work was conducted as part of the in-house research of the Air Force Research Laboratory’s Materials and Manufacturing Directorate. The experimental assistance of P.Fagin is gratefully acknowledged. Two of the authors (SLS, NCL) were supported under the auspices of Air Force Contract FA8650-21-D-5270.

CONFLICT OF INTEREST

On behalf of all authors, the corresponding author states that there is no conflict of interest.

APPENDIX A

Flow-localization calculations were performed to quantify the degree of strain non-uniformity during diffuse necking in the CSCHR test and whether such non-uniformity could affect $\ln \dot{\epsilon}$ -vs- $1000/T(K)$ plots. Simulations were performed using a load-equilibrium analysis of the sheet tension test^[33] under conditions of

constant heating rate and constant true axial stress. For this purpose, symmetry about the mid-length of the sample was assumed, and the reduced section of the half sample was discretized into 10 1-mm-long slices. The width of the sample was tapered assuming a geometry “defect” corresponding to a 2-pct. area deficiency from the sample end to its mid-length. Neglecting the effect of texture for simplicity, a phenomenological stress-strain curve was used to describe the material constitutive behavior, *viz.*,

$$\sigma = C\dot{\epsilon}^m \exp\left(\frac{mQ_{app}}{RT}\right). \quad [A1]$$

Here, all of the symbols have meanings identical to those in Eq. [2] in Section IV-A.

The boundary conditions comprised (1) a constant heating rate (= 75 °C/min) and (2) a constant true stress (= 175 MPa). The latter was imposed by reducing the load during tensile deformation in direct proportion to the cross-sectional area. Two different methods of quantifying the cross-sectional area were used in the simulations, both of which gave identical results in terms of strain profiles, $\ln \dot{\epsilon}$ -vs- $1000/T(K)$ plots, etc. As in the actual experiments, the first method focused on the overall (instantaneous) axial extension/reduced-section length and the calculation of the area based the constant-volume assumption. The second comprised determining the average area of the 10 slices used in each simulation.

Simulations were performed using different combinations of the materials coefficients (all of which were taken to be temperature independent), the most important being the values of m . Irrespective of the specific value of m (which determined the kinetics of evolution of the diffuse neck and its transition into a localized neck), all of the predictions showed similar behaviors, and thus the results for only one case are summarized here, *i.e.*, $m = 0.18$, $C = 4 \text{ MPa s}^{0.18}$, and $Q_{app} = 250 \text{ kJ/mol}$. Figure A1(a) shows the simulated $\ln \dot{\epsilon}$ -vs- $1000/T(K)$ behavior (solid green line), for which $\dot{\epsilon}$ was determined from predictions of the overall axial strain ($\epsilon = \ln(L/L_0)$, in which L and L_0 denote the instantaneous and initial sample length, respectively) as a function of time. For values of $1000/T$ greater than approximately 0.85, the behavior is linear with a slope ($Q/R = 30,070 \text{ K}$) that matches that deduced from an Arrhenius plot of Eq. [A1] assuming a constant value of stress σ (= 175 MPa).

Simulation predictions of the corresponding axial strain profiles (*i.e.*, local strain vs axial position Z) quantified the degree of strain non-uniformity (Figure A1(b)). For $(1000/T) \geq 0.85$ (overall axial strains of 0.05, 0.20, and 0.35), the strain gradient was low. For $(1000/T) < 0.85$, on the other hand, a sharp upturn in the $\ln \dot{\epsilon}$ -vs- $1000/T(K)$ plot (Figure A1(a)) and a marked strain gradient (data for overall axial strain = 0.60), indicative of the loss of quasi-stable flow and the onset of localized flow, were predicted. Thus, such upturns could be used as an indicator of the point at

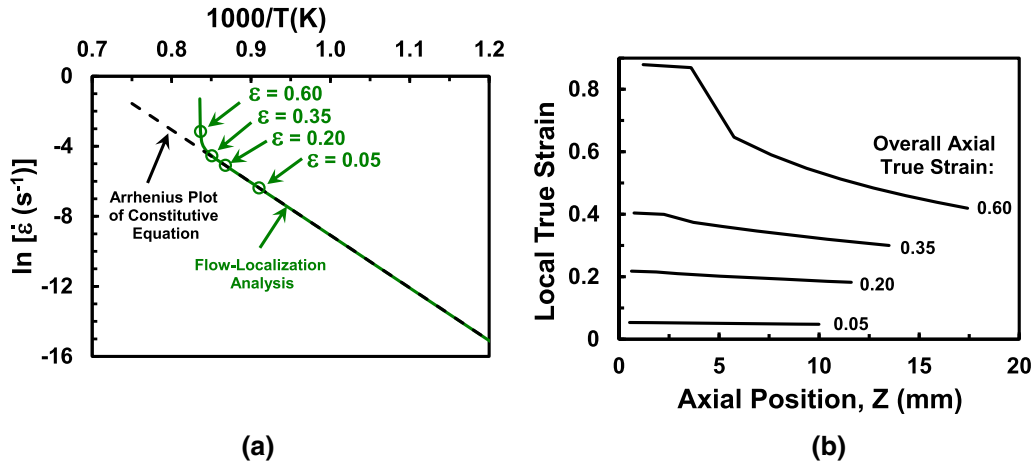


Fig. A1—Flow-localization-simulation predictions for CSCHR tension testing of a sheet sample with a geometry defect of 2 pct., heating rate = 75 °C/min, stress = 175 MPa, and constitutive parameters comprising $m = 0.18$, $C = 4 \text{ MPa s}^{0.18}$, and $Q_{\text{app}} = 250 \text{ kJ/mol}$: (a) $\ln \dot{\epsilon}$ -vs- $1000/T$ and (b) axial strain profiles for overall strains $\epsilon = 0.05, 0.20, 0.35$, and 0.60 .

which $\ln \dot{\epsilon}$ -vs- $1000/T(K)$ measurements should be disregarded in CSCHR measurements.

The results also showed that the onset of localized flow in CSCHR tests corresponds closely to that predicted in flow-localization models for deformation under *isothermal* conditions.^[34] In such cases, the so-called limit (true) strain (ϵ_f) is given by the expression

$$\epsilon_f = -m \ln(1 - f_o^{1/m}), \quad [\text{A2}]$$

in which the geometric defect/area deficiency is represented by the factor $1-f_o$. For $1-f_o = 0.02$, $f_o = 0.98$, and the limit strain is equal to 0.22, 0.40, or 0.57 for $m = 0.12, 0.18$, or 0.23 . Hence, estimates of the m value can provide a useful first-order guide for the maximum strains that can be imposed during CSCHR testing.

APPENDIX B

To assess the relative contribution of deformation of the alpha phase to the overall flow stress of Ti64, the evolution of its volume fraction (f_α) during the heating cycle of CSCHR testing and subsequent moderate-rate cooling following testing in the vacuum furnace used in the present research was modeled. For both heating and cooling stages, relatively simple one-dimensional, mean-field diffusion calculations (incorporating soft impingement of adjacent concentration fields) similar to those in prior work^[21,35-37] were utilized. In both cases, the dissolution (during heating) or re-growth (during cooling) assumed a dispersion of mono-sized spheres. Input data included phase equilibria for Ti64 (equilibrium phase fractions and phase compositions as a function of temperature^[36]), measured values for the initial radius ($7.0 \mu\text{m}$) and volume fraction (0.92) of alpha particles, the heating rate (75 °C/min), cooling rate after fracture (55 °C/min), and the diffusivity of the rate-limiting solute, which was taken to be vanadium, *i.e.*, D_V . For the diffusivity, two dependences on temperature were used, one typical of that for

substitutional diffusion in an annealed matrix (so-called static diffusivity) and the other for diffusion in a matrix that is undergoing concurrent deformation such as occurs during CSCHR deformation (so-called dynamic diffusivity), *viz.*,

$$\text{Static : } D_V(\mu\text{m}^2/\text{s}) = 1.5 \times 10^5 \exp[-17461/T(\text{K})] \quad [\text{B1}]$$

$$\text{Dynamic : } D_V(\mu\text{m}^2/\text{s}) = 12 \times 10^5 \exp[-17461/T(\text{K})]. \quad [\text{B2}]$$

The only major difference between the present and prior calculation approaches concerned the development of a method to couple the output of the dissolution (on-heating) simulation to the input of the re-growth (on-cooling) simulation. As described in Reference 37, during dissolution, vanadium diffuses down a concentration gradient toward the alpha particle(s), whereas during growth, it diffuses down a concentration gradient leading away from the alpha particle(s). During the transition from heating to cooling, a region of zero concentration gradient and hence flux is produced close to the alpha-beta interface. Mean-field diffusion analyses cannot treat such transients. Therefore, a simple method was developed in the present work to initiate the simulation of *growth* during cooling. It comprised the determination of the approximate time required to homogenize the concentration field between adjacent alpha particles. For a specified cooling rate, the temperature to begin the re-growth simulation was thus determined.

Simulation predictions of f_α for the coupled dissolution/re-growth problem using the dynamic diffusivity (for dissolution) during heating and the static diffusivity (for re-growth) during cooling are summarized in Figure B1. The predicted value of f_α at the end of the heating *and* cooling cycle showed very good agreement with that measured on an actual test sample, thereby

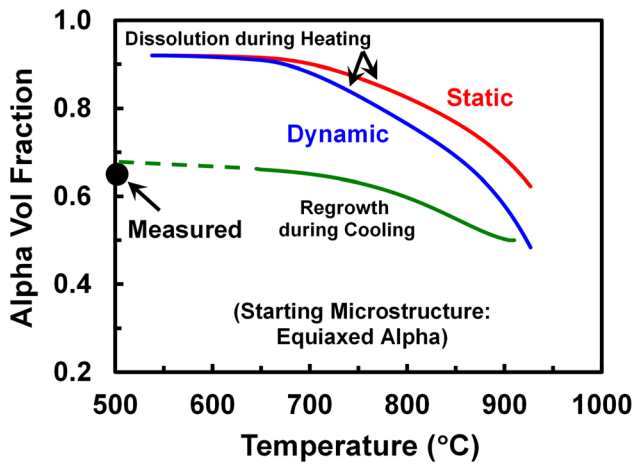


Fig. B1—Simulation predictions of the volume fraction of equiaxed alpha developed during CSCHR testing, including both dissolution during heating and re-growth during cooling. The plot also shows the volume fraction of alpha measured at the end of the heating/cooling cycle.

providing confidence in the accuracy of the modeling technique to quantify the overall transient magnitude of f_{α} . For comparison purposes, the corresponding heating simulation using the static diffusivity for vanadium is also shown in Figure B1. As expected, dissolution predictions using the dynamic vs the static diffusivities indicated substantial differences.

REFERENCES

1. W.A. Backofen: *Deformation Processing*, Addison-Wesley, Reading, 1972.
2. W.F. Hosford and W.A. Backofen: *Fundamentals of Deformation Processing*, Syracuse University Press, Syracuse, 1964, pp. 259–98.
3. U.F. Kochs, C.N. Tome, and H.-R. Wenk: *Texture and Anisotropy*, Cambridge University Press, Cambridge, 1998.
4. K. Ankamma, D.V.V. Satyanarayana, G. Chandramohan Reddy, M. Komaraiah, and N. Eswara Prasad: *Sadhana*, 2011, vol. 36 (#2), pp. 223–49.
5. R.L. Whiteley: *Trans. ASM*, 1960, vol. 52, pp. 154–64.
6. S. Basak, S.K. Panda, and M-G. Lee: *Inter. J. Mech. Sci.*, 2020, vol. 170, paper 105346.
7. Z. Marciniak and K. Kuczynski: *Inter. J. Mech. Sci.*, 1967, vol. 9, pp. 609–20.
8. F. Larson and A. Zarkades: *Properties of Textured Titanium Alloys*, Report MCIC 74-20, Metals and Ceramics Information Center, Battelle's Columbus Laboratories, Columbus, OH, 1974.
9. A.A. Salem, M.G. Glavicic, and S.L. Semiatin: *Mater. Sci. Eng. A*, 2008, vol. A496, pp. 169–76.
10. D. Lee: *Trans. TMS-AIME*, 1966, vol. 235, pp. 1077–84.
11. D. Lee and W.A. Backofen: *TMS-AIME*, 1966, vol. 236, pp. 1696–1704.
12. S.L. Semiatin and T.R. Bieler: *Metall. Mater. Trans. A*, 2001, vol. 32A, pp. 1787–99.

13. O. Kaibyshev, I.V. Kazachkov, and R.M. Galeev: *J. Mater. Sci.*, 1981, vol. 16, pp. 2501–06.
14. L. da Silva, G. Sivaswamy, L. Sun, and S. Rahimi: *Mater. Sci. Eng. A*, 2021, vol. A819, paper 141367.
15. P.G. Partridge, D.S. McDermid, and A.W. Bowen: *Acta Metall.*, 1985, vol. 33, pp. 571–77.
16. A.W. Bowen, D.S. McDermid, and P.G. Partridge: *J. Mater. Sci.*, 1991, vol. 26, pp. 3457–62.
17. D.V. Dunford, A. Wisbey, and P.G. Partridge: *Mater. Sci. Technol.*, 1991, vol. 7, pp. 62–70.
18. C. Cheng, Z. Chen, H.E. Li, X. Wang, S. Zhu, and Q. Wang: *Mater. Sci. Eng. A*, 2021, vol. A800, paper 140362.
19. W. Li, Z. Chen, J. Liu, Q. Wang, and G. Sui: *Mater. Sci. Eng. A*, 2017, vol. A688, pp. 322–29.
20. S.L. Semiatin, P.N. Fagin, N.C. Levkulich, B.T. Gockel, B.F. Antolovich, E.M. Crist, J. Cormier, and J.S. Tiley: *Metall. Mater. Trans. A*, 2022, vol. 53A, pp. 394–406.
21. S.L. Semiatin, N.C. Levkulich, C.A. Heck, A.E. Mann, N. Bozzolo, A.L. Pilchak, and J.S. Tiley: *Metall. Mater. Trans. A*, 2020, vol. 51A, pp. 2291–2305.
22. O.I.M. Analysis: *Version 8.0*, EDAX Corporation, Mahwah, 2016.
23. L. Briottet, J.J. Jonas, and F. Montheillet: *Acta Mater.*, 1996, vol. 44, pp. 1665–72.
24. N.E. Paton and W.A. Backofen: *Metall. Trans.*, 1970, vol. 1, pp. 2839–47.
25. J.C. Williams, R.G. Baggerly, and N.E. Paton: *Metall. Mater. Trans. A*, 2002, vol. 33A, pp. 837–50.
26. S.L. Semiatin, F. Montheillet, G. Shen, and J.J. Jonas: *Metall. Mater. Trans. A*, 2002, vol. 33A, pp. 2719–27.
27. S.L. Semiatin and G.D. Lahoti: *Metall. Trans. A*, 1981, vol. 12A, pp. 1705–17.
28. A.K. Ghosh and R.A. Ayres: *Metall. Trans. A*, 1976, vol. 7A, pp. 1589–91.
29. D.A. Woodford: *Trans. ASM*, 1969, vol. 62, pp. 291–93.
30. P.D. Nicolaou, A.K. Ghosh, and S.L. Semiatin: in *Fundamentals of Modeling for Metals Processing*, *ASM Handbook, Volume 22A*, D.U. Furrer and S.L. Semiatin, eds., ASM International, Materials Park, OH, 2009, pp. 325–38.
31. P.D. Nicolaou, S.L. Semiatin, and A.K. Ghosh: *Metall. Mater. Trans. A*, 2000, vol. 31A, pp. 1425–34.
32. P.D. Nicolaou, A.K. Ghosh, and S.L. Semiatin: *Metall. Mater. Trans. A*, 2004, vol. 35A, pp. 2187–90.
33. S.L. Semiatin, A.K. Ghosh, and J.J. Jonas: *Metall. Trans. A*, 1985, vol. 16, pp. 2291–98.
34. S.L. Semiatin and J.J. Jonas: *Formability and Workability of Metals: Plastic Instability and Flow Localization*, American Society for Metals, Metals Park, 1984.
35. S.L. Semiatin, M. Obstalecki, E.J. Payton, A.L. Pilchak, P.A. Shade, N.C. Levkulich, J.M. Shank, D.C. Pagan, F. Zhang, and J.S. Tiley: *Metall. Mater. Trans. A*, 2019, vol. 50A, pp. 2356–70.
36. S.L. Semiatin, S.L. Knisley, P.N. Fagin, F. Zhang, and D.R. Barker: *Metall. Mater. Trans. A*, 2003, vol. 34A, pp. 2377–86.
37. M. Kulakov, S. Rahimi, and S.L. Semiatin: *Metall. Mater. Trans. A*, 2022, vol. 53A, pp. 407–19.

Publisher's Note Springer Nature remains neutral with regard to jurisdictional claims in published maps and institutional affiliations.

Springer Nature or its licensor (e.g. a society or other partner) holds exclusive rights to this article under a publishing agreement with the author(s) or other rightsholder(s); author self-archiving of the accepted manuscript version of this article is solely governed by the terms of such publishing agreement and applicable law.